Three-Dimensional Viscous Rotor Flow Calculations Using a Viscous–Inviscid Interaction Approach

Ching S. Chen, Ames Research Center, Moffett Field, California
John O. Bridgeman, Woodside Summit Group, Inc., Mountain View, California

February 1990

NOMENCLATURE

a_∞ = ambient speed of sound

c = root chord length

C_p = nondimensional specific heat coefficient

h = nondimensional time step in full-potential method

H = nondimensional total enthalpy

J = grid Jacobian

M_1, M_2 = Mach number upstream and downstream of a shock

p_∞ = ambient pressure

p = nondimensional pressure

R = perfect gas constant

s_1, s_2 = entropy upstream and downstream of a shock

t = nondimensional time in full-potential method

T = nondimensional temperature

u_e = nondimensional tangential velocity on body surface in full-potential method

u, v, w = nondimensional velocities in x, y, z directions

U, V, W = contravariant velocities

V_δ = transpiration velocity

x, y, z = rotor blade coordinate system; x—parallel to blade chord, y—normal to blade surface, z—parallel to blade radius

β = $p_\infty / (p_\infty a_\infty^2)$

γ = ratio of specific heats

δ^* = displacement thickness

iii

μ	= nondimensional viscosity, the sum of molecular and eddy viscosities
ξ, η, ζ	= transformed rotor blade coordinate system; ξ—parallel to blade chord, η—normal to blade surface, ζ—parallel to blade radius
ρ	= nondimensional density
ρ_c	= nondimensional density on body surface in full-potential method
ρ_i	= nondimensional isentropic density
ρ_∞	= ambient density
τ	= shear stress
ϕ	= velocity potential
ω	= relaxation parameter in boundary-layer method
Ω^*	= tip Mach number/aspect ratio
δs	= entropy difference
∂d	= distance along body surface
n	= time step for full-potential method

SUMMARY

A three-dimensional viscous–inviscid interaction analysis has been developed to predict the performance of rotors in hover and in forward flight at subsonic and transonic tip speeds. The analysis solves the full-potential and boundary-layer equations by finite-difference numerical procedures. Calculations were made for several different model rotor configurations. The results were compared with predictions from a two-dimensional integral method and with experimental data. The comparisons show good agreement between predictions and test data.

INTRODUCTION

The ability to accurately predict performance is important in the design of rotorcraft. Advancements in computational fluid dynamics now allow some complex rotor performance predictions to be performed routinely to help guide engineers in the design process. There are several different levels of complexity in the methods available for this purpose. Their use depends upon the flow field information needed by the designer. The more complex methods provide more detailed information about the flow field, but in general are more expensive computationally.

The prediction methods range in complexity from simple lifting-line theory, to lifting-surface theory, to sophisticated finite difference methods (small-disturbance, full-potential, Euler, and Navier-Stokes). Only the Navier-Stokes method can predict viscous drag directly. However, this method requires large computer memory and long CPU times. The other methods rely on either (1) two-dimensional airfoil tables or (2) approximate methods to predict the viscous drag. There are several problems with the first approach. First, two-dimensional airfoil data does not model the highly three-dimensional flow behavior at the tip region, because of complex tip shapes or transonic flow unsteadiness in forward flight. Second, it does not take the variations in Reynolds number or the rotational effects of the blade into account. Third, for airfoils yet to be tested, the results may be dubious.

Adopting the second approach, Bridgeman et al. [1] incorporated a two-dimensional integral boundary-layer method, the Nash–MacDonald scheme [2], into a full-potential finite-difference method to predict the viscous drag directly. The advantage of this approach is that it is fast-running, easy to implement, and fairly robust for attached boundary-layer flows. The disadvantage is that it cannot handle three-dimensional flow phenomena at the blade tip, and for flows with separation the results are less certain. One possibility for solving these problems is the incorporation of three-dimensional boundary-layer equations into the analysis.

In the present study, a three-dimensional boundary-layer finite-difference method is coupled with a full-potential finite-difference method to form a viscous–inviscid interaction analysis (V–II). (The boundary-layer method [3], BL3D, was originally developed by Van Dalsem and Steger for applications in fixed-wing flows. The full-potential method was developed by Strawn et al. [4] for inviscid rotor flows.) V–II was developed to make rotor performance predictions efficiently for general rotor configurations without the above-mentioned problems.

The accuracy of BL3D was first evaluated by simulating flows over a flat plate and two-dimensional airfoils. A comparison of theoretical and experimental data shows good accuracy of the method. V–II was then used to calculate nonlifting model rotor flows in hover and forward flight. The agreement between predictions and test data demonstrates the capability of this method.

The computational efforts for rotor flows were concentrated on nonlifting flows for both hover and forward flight, because (1) it is not possible to measure viscous drag directly in lifting flows and (2) the influences due to rotor wake can be minimized. In lifting rotor flows, the wake shed by the blades plays a very important role in the performance prediction. Viscous drag is only 20%-30% of the total drag. A slightly different wake geometry could alter the pressure drag by 10%. Wake geometry prediction, especially for advanced rotor configurations, is still in the development stage.

VISCOUS FORMULATION—BOUNDARY-LAYER METHOD

In the boundary-layer method the unsteady, three-dimensional, compressible boundary-layer equations are solved in a rotating reference frame. A general x, y, z to $\xi(x, z), \eta(x, y, z), \zeta(x, z)$ coordinate transformation is used to avoid a complex similarity transformation. The two sets of coordinate systems are shown in Fig. 1.

Boundary-Layer Equations

Neglecting surface curvature, the nondimensional boundary-layer equations for a perfect gas can be written in $\xi(x, z), \eta(x, y, z), \zeta(x, z)$ coordinates as follows [3]:

x-momentum equation

$$\rho u_t + \rho(U u_\xi + V u_\eta + W u_\zeta - 2w\Omega^* - x(\Omega^*)^2) = -\beta(p_\xi \xi_x + p_\zeta \zeta_x) + (\mu u_\eta \eta_y)_\eta \eta_y \tag{1}$$

z-momentum equation

$$\rho w_t + \rho(U w_\xi + V w_\eta + W w_\zeta + 2u\Omega^* - z(\Omega^*)^2) = -\beta(p_\xi \xi_z + p_\zeta \zeta_z) + (\mu w_\eta \eta_y)_\eta \eta_y \tag{2}$$

perfect gas relation

$$\rho = \rho T \tag{3}$$

energy equation (H = total enthalpy)

$$H \equiv C_p T + \frac{1}{2}(u^2 + v^2 + w^2) = CONSTANT \tag{4}$$

2

continuity equation

$$\rho_t + (\rho u)_\xi \xi_x + (\rho u)_\eta \eta_x + (\rho u)_\zeta \zeta_x + (\rho v)_\eta \eta_y + (\rho w)_\xi \xi_z + (\rho w)_\eta \eta_z + (\rho w)_\zeta \zeta_z = 0 \qquad (5)$$

and

$$\begin{bmatrix} U \\ V \\ W \end{bmatrix} = \begin{bmatrix} \xi_t + \xi_x u + \xi_z w \\ \eta_t + \eta_x u + \eta_y v + \eta_z w \\ \zeta_t + \zeta_x u + \zeta_z w \end{bmatrix} \qquad (6)$$

where U, V, and W are unscaled contravariant velocities, $\Omega^* = $ tip Mach number/aspect ratio, $\beta = p_\infty / (\rho_\infty a_\infty^2)$, and a_∞ is the ambient speed of sound.

Viscosity, pressure, temperature, and density are nondimensionalized by the ambient values. The velocities u and w are nondimensionalized by the ambient speed of sound. The coordinates x and z are nondimensionalized by a characteristic length, typically the chord length at the blade root. The v and y variables are nondimensionalized by the same quantities divided by $\sqrt{Re_\infty}$. For turbulent flows, the viscosity is the sum of the molecular and eddy viscosities. The eddy viscosity is evaluated by Cebeci's two-layer algebraic turbulence model [5].

Of note are the four terms $2w\Omega^*, x(\Omega^*)^2, 2u\Omega^*$, and $z(\Omega^*)^2$ in the x- and z-momentum equations. They represent Coriolis and centrifugal forces in the boundary layer induced by the rotation of the blade.

Solution Algorithm

A relaxation algorithm [3] is used to solve the boundary-layer equations. The advantages of using relaxation rather than space marching are that relaxation is easier to implement, and simpler boundary conditions can be specified. For example, it would be very difficult to specify the flow quantities at the tip of the blade, as required by a space marching algorithm. In a relaxation algorithm, a zero or first-order boundary condition can be used with local grid mesh refinement to minimize the impact on the final results [3].

The pressure terms in equations (1) and (2) are treated as known functions. The boundary-layer equations are weakly coupled and can be solved sequentially at each time (or iteration) step. As a result, a semi-implicit scheme is used at each time step. The time derivatives are approximated with a first-order accurate, forward-difference operator. The space derivatives in the direction normal to the body are approximated with a second-order accurate, central-difference operator; and second-order accurate, backward-difference operators are used for the other two directions.

The FLARE approximation [6] is employed in the reversed flow regions in the streamwise direction. That is, the streamwise convection term is dropped out if the streamwise velocity is negative. This is justified by the fact that the streamwise velocity in the reversed flow regions is small, usually less than

3

10% of the maximum velocity found in the viscous region [6]. In the continuity equation, the derivatives in the ξ and ζ directions are approximated with second-order central-difference operators, and trapezoidal-rule integration is used in the η direction to calculate the v velocity.

The typical grid mesh [7] used by BL3D for the calculations in this paper is 40 points in the chordwise direction, 16 in the spanwise direction, and 50 in the direction normal to the blade surface. The upper and lower surfaces of the blade are calculated separately. The computation starts a small distance away from the stagnation point at the leading edge. The flow velocities at the initial plane are assumed to have known values, and are obtained by solving the Falkner–Skan similarity equations [8]. At each time step the computation starts from the initial plane, sweeps through the grid mesh, and ends at the trailing edge. A first-order boundary condition is used at the trailing edge. The wake was not included in the calculations.

The solution algorithm for flows with a strong shock or a major separation is not very robust. Our experience shows that the boundary-layer method is very sensitive to the large adverse pressure gradient at the shock or the trailing edge. In calculating flows with a strong shock, typically when the tip Mach number is greater than 0.92, the shock must be smoothed to prevent the computation from diverging. However, since rotors are seldom operated with tip Mach numbers this large, this problem has little practical significance. The trailing-edge stagnation point is another persistent problem. An O grid is used in the full-potential method, and it seems that the adverse pressure gradient predicted is too large. Our experience shows that pressure smoothing, along with a transpiration flux limiter, which prevents the excessive boundary-layer growth from destabilizing the potential flow, must be applied at the trailing edge to prevent the solutions from diverging, even in flows with low tip Mach number. In all calculations, fully turbulent flow was assumed.

INVISCID FORMULATION—FULL-POTENTIAL METHOD

The inviscid flow is assumed to be isentropic, inviscid, and irrotational. These assumptions are suitable for a wide range of transonic flows. For flows with a strong shock, a nonisentropic correction is added to the formulation to account for the entropy produced at the shock.

Equations

The unsteady, three-dimensional, full-potential equation in strong conservation form is written in generalized coordinates as [4]

$$\frac{\partial}{\partial \tau}\left(\frac{\rho}{J}\right) + \frac{\partial}{\partial \xi}\left(\frac{\rho U}{J}\right) + \frac{\partial}{\partial \eta}\left(\frac{\rho V}{J}\right) + \frac{\partial}{\partial \zeta}\left(\frac{\rho W}{J}\right) = 0 \tag{7}$$

with density given by

$$\rho = \{1 + \frac{\gamma-1}{2}[-2\phi_t - (U + \xi_t)\phi_\xi - (V + \eta_t)\phi_\eta - (W + \zeta_t)\phi_\zeta]\}^{\frac{1}{\gamma-1}} \tag{8}$$

4

where

$$U = \xi_t + A_1\phi_\xi + A_4\phi_\eta + A_5\phi_\zeta$$

$$V = \eta_t + A_4\phi_\xi + A_2\phi_\eta + A_6\phi_\zeta \tag{9}$$

$$W = \zeta_t + A_5\phi_\xi + A_6\phi_\eta + A_3\phi_\zeta$$

and

$$A_1 = \xi_x^2 + \xi_y^2 + \xi_z^2$$

$$A_2 = \eta_x^2 + \eta_y^2 + \eta_z^2$$

$$A_3 = \zeta_x^2 + \zeta_y^2 + \zeta_z^2$$

$$A_4 = \xi_x\eta_x + \xi_y\eta_y + \xi_z\eta_z \tag{10}$$

$$A_5 = \xi_x\zeta_x + \xi_y\zeta_y + \xi_z\zeta_z$$

$$A_6 = \eta_x\zeta_x + \eta_y\zeta_y + \eta_z\zeta_z$$

In the above equations, ρ is the fluid density, U, V, and W are contravariant velocities, and J is the grid Jacobian. The velocity potential is given by ϕ, and the generalized coordinates are ξ, η, ζ and t. All velocities are normalized by the ambient speed of sound, a_∞, distances by the root chord length, c, and time by the combination (c/a_∞). Density is normalized by the free-stream value ρ_∞.

Density Correction for Nonisentropic Flow

A nonisentropic Bernoulli relation is used for density [4]:

$$\rho = \rho_i e^{-\Delta s/R} \tag{11}$$

where ρ_i is the isentropic density given by equation (8).

The entropy correction to the density is made at the half-point just downstream of the shock. The Rankine–Hugoniot equation is used to calculate the entropy change across the shock [9]:

$$\frac{\Delta s}{R} = \frac{s_2 - s_1}{R} = \frac{\gamma}{\gamma - 1} \ln\left[\frac{2}{(\gamma + 1)M_i^2} + \frac{\gamma - 1}{\gamma + 1} \right] + \frac{1}{\gamma - 1} \ln\left[\frac{2\gamma}{(\gamma + 1)} M_i^2 - \frac{\gamma - 1}{\gamma + 1} \right] \tag{12}$$

5

where R is the perfect gas constant, and the subscripts 1 and 2 denote the upstream and downstream conditions of a shock, respectively.

Solution Algorithm

Equation (7) is solved by using first-order backward differencing in time and second-order central differencing in space. The temporal density derivative is locally linearized about the old time levels in a manner that preserves the conservative form [10]. The resulting equation is approximately factored into ξ, η, and ζ operators:

$$L_\xi L_\eta L_\zeta (\phi^{n+1} - \phi^n) = RHS \tag{13}$$

where

$$L_\xi = \left[I + hU^n \delta_\xi - \frac{h^2}{\hat{\beta}^n} \delta_\xi (\hat{\rho} A_1)^n \delta_\xi \right]$$

$$L_\eta = \left[I + hV^n \delta_\eta - \frac{h^2}{\hat{\beta}^n} \delta_\eta (\hat{\rho} A_2)^n \delta_\eta \right] \tag{14}$$

$$L_\zeta = \left[I + hW^n \delta_\zeta - \frac{h^2}{\hat{\beta}^n} \delta_\zeta (\hat{\rho} A_3)^n \delta_\zeta \right]$$

and

$$RHS = \frac{h^2}{\hat{\beta}^n} \left[\delta_\xi (\hat{\rho} U)^n + \delta_\eta (\hat{\rho} V)^n + \delta_\zeta (\hat{\rho} W)^n - R \right] + C \tag{15}$$

which represents central difference operators in space. The term C is given by

$$C = \left[I + h \frac{\hat{\beta}^{n-1}}{\hat{\beta}^n} \left(U^{n-1} \delta_\xi + V^{n-1} \delta_\eta + W^{n-1} \delta_\zeta \right) \right] \left(\phi^n - \phi^{n-1} \right)$$

$$+ \frac{\hat{\beta}^{n-1}}{\hat{\beta}^n} \left(\phi^n - 2\phi^{n-1} + \phi^{n-2} \right) + \frac{h}{\hat{\beta}^n} \left(\hat{\rho}^n - \hat{\rho}^{n-1} \right) \tag{16}$$

The bracketed term in equation (16) represents the temporal conservation in the algorithm. In the above equations, h is the difference of two consecutive time steps, $\hat{\beta} = \rho^{2-\gamma} / J$ and $\hat{\rho} = \rho / J$. The superscript n represents the time step.

6

A steady state ADI relaxation algorithm can be obtained from equation (13) by omitting the unsteady C term on the right-hand side of the equation, adding temporal dissipation in the ξ direction, and allowing for a time-stepping sequence for accelerated convergence.

The basic grid system is composed of a series of parallel chordwise O grids. Body motion is incorporated by assigning an appropriate coordinate velocity $(\xi_\tau, \eta_\tau, \zeta_\tau)$ to each grid point. The coordinate velocity is defined with respect to an inertial coordinate frame. The coordinate velocity can be translational, rotational, or a combination of the two.

The angle-of-attack conditions on the blade surface (including inflow angles induced by the rotor wake) are simulated by a transpiration velocity condition. At the outer radial boundary of the O grid, a nonreflection boundary condition is used to prevent the accumulation of numerical disturbances. Typical grid size for the inviscid calculations in this paper is 80 points in the chordwise direction, 25 in the spanwise direction, and 25 in the direction normal to the rotor surface. The finite difference grid extends approximately 2 chords outward from the rotor tip in the spanwise direction. The outer radial boundary of the O grid is about 5 chords from the blade surface. Variable time steps are used for the steady flows, such as hover, to accelerate convergence.

COUPLING OF VISCOUS AND INVISCID SOLUTIONS

To obtain a meaningful solution, the viscous–inviscid interaction must allow each flow to influence the other. The classical way of introducing viscous effects into an inviscid flow is to add displacement thickness to the body surface. When this is done the geometry of the body and therefore the grids must be recomputed after each iteration. This is computationally costly. A more efficient and robust alternative is to impose a transpiration velocity at the body surface, as first suggested by Lighthill [11].

Viscous–Inviscid Interaction

In this approach the original flow tangency condition in the inviscid flow is modified by enforcing a normal velocity component on the body. A flowchart depicting the viscous–inviscid interaction process is shown in Fig. 2. The normal velocity component (i.e., the transpiration velocity) deflects the inviscid flow from the body surface, thus simulating the displacement of the inviscid flow due to the momentum defect in the boundary layer. The transpiration velocity due to the boundary layer is given by

$$V_\delta = \frac{1}{\rho_e} \frac{\partial\left(\rho_e u_e \delta^*\right)}{\partial d} \tag{17}$$

where ρ_e and u_e are the inviscid density and the tangential velocity on the body surface, δ^* is the displacement thickness, and d is the distance along the body surface.

Depending upon the application, it is sometimes not necessary to recompute viscous flow after each inviscid iteration because the inviscid flow does not change much between iterations. In order to speed

up the convergence, the ratio of inviscid to viscous iterations was set to five for all hover calculations. For forward flight calculations, however, the ratio was set to one because the computation was unsteady.

Viscous–Inviscid Interaction: Direct and Inverse Modes

Depending upon the flow conditions, the inviscid solution can be incorporated into the boundary-layer equations in one of two ways. If the flow is fully attached, i.e., there is no separation, the boundary-layer equations can be solved directly with pressures provided by the full-potential method. This direct-mode solution process is straightforward. If the flow separates, however, the direct mode cannot be used, because (1) there is a singularity at the separation point and (2) flow reversal prohibits computing the solution in the direction of the external flow unless the convection terms in the momentum equations are altered [6]. An inverse mode is needed in this case. In the inverse mode, wall shear stress and wake centerline velocity are treated as the forcing functions in the momentum equations, and pressure becomes part of the solution [7].

To solve the boundary-layer equations in the inverse mode, the algorithm must be modified so that the inverse forcing functions can be specified. This is achieved by replacing the pressure terms in the momentum equations with the inverse forcing functions. These relations are obtained by applying the momentum equations to the body surface or the wake centerline. For example, applying the x-momentum equation to the body surface yields

$$\beta(p_\xi \xi_x + p_\zeta \zeta_x) = \rho(2w\Omega^* + x(\Omega^*)^2) + \left[(\mu u_\eta \eta_y)_\eta \eta_y\right]_{wall} \tag{18}$$

After the boundary-layer equations are solved in the inverse mode at each iteration, the pressure is calculated by assuming that the fluid is an isentropic perfect gas.

A shear stress distribution is first assumed for the proposed separated regions at the beginning of the computation and is then updated by the following equation:

$$\tau^{n+1} = \tau^n + \omega(p_{viscous} - p_{inviscid}) \tag{19}$$

This update is continued until the pressure predicted by the viscous method matches that of the inviscid method. The term ω is a relaxation parameter; a value of 0.1 was used in most of the calculations.

Currently, the inverse mode can be applied only in one direction, usually streamwise. This restriction is due to the fact that in the inverse mode the wall shear stress or the wake centerline velocity is updated by the inviscid and viscous pressure difference. If the inverse mode is applied in both streamwise and spanwise directions then the pressure will have to be calculated in these two directions during the same iteration. The pressure calculated in the spanwise direction will not be the same as that calculated in the chordwise direction. The question then arises, which pressure, chordwise or spanwise, should be used to update the inverse forcing function as described in Equation (19). Further study is needed to ensure that this double-updating process would not cause convergence problems before implementation.

RESULTS AND DISCUSSION

Flat Plate Flows

Before the coupled V–II code was run, an attempt was made to validate the accuracy of BL3D by itself. This was accomplished by computing both laminar and turbulent flows over a flat plate. The Reynolds number for the laminar flow was 10^5. The computed local friction coefficients are compared with the analytical results derived from a Blasius solution [12] in Fig. 3. The agreement is excellent. For the turbulent flow, the Reynolds number was 10^6. The computed local friction coefficients are compared with experimental data [12] in Fig. 4. The friction coefficient calculated by BL3D is consistently low by about 10%. This error is believed to be a result of an inaccuracy in Cebeci's turbulence model which was used for the calculation.

Two-Dimensional Airfoil Flows

V–II was then used to compute nonlifting, two-dimensional airfoil flows with a NACA 0012 airfoil. Flows with two different Reynolds numbers, 10^6 and 10^7, and a Mach number range of 0.3 to 0.8 were computed. In these computations the aspect ratio of the blade was set very large, at 10,000, such that a few chords away from the tip the flows were essentially two-dimensional, and the flows were assumed to be fully turbulent. The computed drag coefficients are compared with experimental data [13] for the lower-Reynolds-number flow, 10^6, in Fig. 5. The agreement is very good, with the computed drag coefficients well within the test band. V–II predicts a drag rise Mach number of 0.77, which is confirmed by the experimental data.

A similar comparison is made for the higher-Reynolds-number flow in Fig. 6. The predicted drag coefficients were slightly lower than the experimental values. Again, the discrepancy is believed to be a result of inaccuracies in Cebeci's turbulence model. But since only one turbulence model is used in V–II, no definite conclusion can be drawn here. V–II again predicts a drag rise Mach number of 0.77, which is consistent with the experimental data [13]. Note that V–II predicts higher-magnitude drag coefficients for lower-Reynolds-number flows, as anticipated.

The solutions of version 1 of the full-potential code [1] had a large pressure drag tare, about eighty counts. Theoretically, an object should experience no drag if the flow is inviscid and subsonic. The numerical algorithm was improved to reduce the tare value, as described in [4], but a small tare value still exists. This tare value for subsonic flows is less than 5% of the value with the Euler method [4]. Its value is less certain in the transonic region because it is mixed with wave drag. The results reported in this paper include the tare value.

Nonlifting, Hovering Rotor Flows

V–II was used to compute the nonlifting, hovering flow for a two-bladed model rotor system. The blade is untwisted and rectangular, with a NACA 0012 section and an aspect ratio of 13.71. Figure 7 shows the comparison of torques calculated by V–II with that of test data for a tip Mach number range of 0.3 to 0.925. The agreement is excellent. Also plotted in this figure are torques calculated using the two-dimensional integral boundary-layer method as described in [4]. This integral boundary-layer

method predicts lower torque in the higher tip Mach number region (greater than 0.7). Fully turbulent flow was assumed in the calculations of both methods.

To validate V–II for advanced rotor configurations, it was used to calculate the flow of another nonlifting, hovering rotor system. This system consisted of two swept, tapered-tip blades with variable airfoil thickness. A detailed description of this rotor can be found in [4]. The torques calculated were compared with those calculated by the integral boundary-layer method and with the test data, as shown in Fig. 8. The comparison shows that torques predicted by V–II are consistently 10%-15% higher than test values for the range of tip Mach numbers considered. The predictions made by the integral method agree well with the test data in the low tip Mach number region (less than 0.7), but the values were lower in the high tip Mach number region (greater than 0.7).

To investigate the differences in the torque predictions made by V–II and the integral method, the spanwise variations in the viscous drag coefficients obtained by BL3D and by the integral method were compared. Figure 9 shows the comparison for the nonlifting, hovering rotor with rectangular blades at a tip Mach number of 0.9. In calculating the viscous drag coefficient, the surface shear component in the outer flow direction was integrated to obtain the drag coefficient. The wave drag due to shock was not included. As shown in Fig. 9, BL3D does predict a higher viscous drag coefficient. The difference is very large in the inboard region and becomes significantly smaller near the tip.

The same comparison was made for the nonlifting, hovering rotor with swept, tapered-tip blades at the same tip Mach number, as shown in Fig. 10. The viscous drag coefficient difference is not as large in the inboard region, as was the case in the previous comparison, but it increases near the tip region. The value of the viscous drag coefficient calculated by the integral method drops rapidly at the tip region. This might be caused by the inability of the integral method, which was developed for two-dimensional flows, to handle the highly three-dimensional flow at the tip region generated by the swept, tapered tip.

In comparing the viscous drag coefficients calculated by BL3D for the rectangular and the swept-tip blades, it can be seen that the drag coefficient drops faster from root to tip on the rectangular blade than on the swept-tip blade. This is caused by the shock strength being greater on the rectangular blade. The reversed-flow region is larger, therefore the drag coefficient is reduced more.

In order to understand the effects of the viscous–inviscid interaction, pressure coefficient distributions obtained from two different sets of calculations are compared. In the first set the pressure coefficient was calculated by the isentropic full-potential analysis alone. In the second set the pressure coefficient was calculated by the viscous–inviscid interaction. The comparison is made for the nonlifting two-bladed model rotor with rectangular tips in hover, as used in the calculations for Fig. 7, over six different spanwise locations, from nondimensional radius 0.820 (Fig. 11a) to 0.998 (Fig. 11f). The tip Mach number was 0.925. In the inboard region the flow is subsonic, and the results predicted by the two sets are quite close. Near the tip region the flow is transonic, the shock is much stronger, and the predictions show some significant differences with regard to the shock. In general, V–II predicts a weaker shock, and the location of the shock is moved slightly upstream. This does not affect the drag force very much, because the streamwise component of pressure is small, but it will change the blade pitching moment significantly, since the vertical component of pressure is large, and this is important in rotor dynamics.

Nonlifting Rotor Flows in Forward Flight

An important issue to be addressed is the applicability of V–II to the prediction of unsteady flows. To demonstrate this applicability, flows about a nonlifting two-bladed model rotor in forward flight was calculated. The blade has an untwisted, rectangular planform, a NACA 0012 section, and an aspect ratio of 7.125. Figure 12 shows comparisons of measured surface pressures [14] with predictions for a tip Mach number of $M_T = 0.763$ and an advance ratio of $\mu = 0.246$, at a radius of $r/R = 0.946$. The unsteady solution is shown for azimuthal intervals of $30°$. V–II predicts a slightly weaker shock at $60°$ and $90°$ of azimuthal angles. The predicted shock strength is slightly higher at $120°$. The predicted shock location is slightly more upstream, at $150°$. In general, V–II demonstrates that it is able to predict the blade surface pressure distribution of an advancing rotor very well.

CONCLUSIONS

V–II has been developed to predict the performance of rotors in hover and forward flight. The viscous drag can be calculated directly to include the variations in Reynolds number and the rotational effects of the blade. Flows over flat plate and two-dimensional airfoil flows were calculated, and the results were compared with test data. The comparison showed good accuracy of the numerical procedure. Three nonlifting model rotor flows, two in hover and one in forward flight, were calculated. The comparison of predictions with test data demonstrates that V–II is able to make accurate performance predictions efficiently for general rotor configurations.

There are two restrictions in applying V–II to rotor flows. First, it can only handle separation in one direction, either radial or chordwise. If the flow separates in one direction, then flow in the other direction is assumed to be attached. Second, V–II is applicable only when the amount of separation is small. If the separation is large, the solution will diverge. More study is needed to overcome these restrictions.

The pressure drag tare in the full-potential method described in the previous section is a result of the numerical scheme and grid mesh used. Further research is being undertaken by the authors in this area. The next step is to extend V–II, described here for nonlifting flow calculations, to the prediction of lifting flows.

REFERENCES

1. J. O. Bridgeman, R. C. Strawn, and F. X. Caradonna. An entropy and viscosity corrected potential method for rotor performance prediction. *AHS 44th A. Forum* (1988).

2. J. F. Nash and A. G. J. Macdonald. The calculation of momentum thickness in a turbulent boundary-layer at Mach numbers up to unity. Aeronautical Research Council C.P. No. 963, London (1967).

3. W. R. Van Dalsem and J. L. Steger. The efficient simulation of separated three-dimensional viscous flows using the boundary-layer equations. AIAA Paper 85-4064 (1985).

4. J. O. Bridgeman, R. C. Strawn, F. X. Caradonna, and C. S. Chen. Advanced rotor computations with a corrected potential method. *AHS 45th A. Forum* (1989).

5. T. Cebeci. Calculation of compressible turbulent boundary-layers with heat and mass transfer. AIAA Paper 70-741 (1970).

6. D. A. Anderson, J. C. Tannehill, and R. H. Pletcher. *Computational Fluid Mechanics and Heat Transfer*. Hemisphere Publishing Corporation, New York (1984).

7. W. R. Van Dalsem. Simulation of separated transonic airfoil flow by finite-difference viscous-inviscid interaction. Ph.D. Dissertation, Stanford University (1984).

8. F. M. White. *Viscous Fluid Flow*. McGraw-Hill Book Company, New York (1974).

9. A. H. Shapiro. *The Dynamics and Thermodynamics of Compressible Fluid Flow; Volume 1*. John Wiley & Sons, Inc., New York (1953).

10. J. O. Bridgeman, J. L. Steger, and F. X. Caradonna. A conservative finite-difference algorithm for the unsteady transonic potential equation in generalized coordinates. AIAA Paper 82-1388 (1982).

11. M. J. Lighthill. On displacement thickness. *J. Fluid Mech.* 4, 383-392, 1958.

12. H. Schlichting. *Boundary Layer Theory*, 7th edn. McGraw-Hill Book Company, New York (1979).

13. W. J. McCroskey. A critical assessment of wind tunnel results for the NACA 0012 airfoil. AGARD CP-429 (1987).

14. F. X. Caradonna, J. L. Lautenschlager, and M. J. Silva. An experimental study of rotor blade-vortex interactions. AIAA Paper 88-0045 (1988).
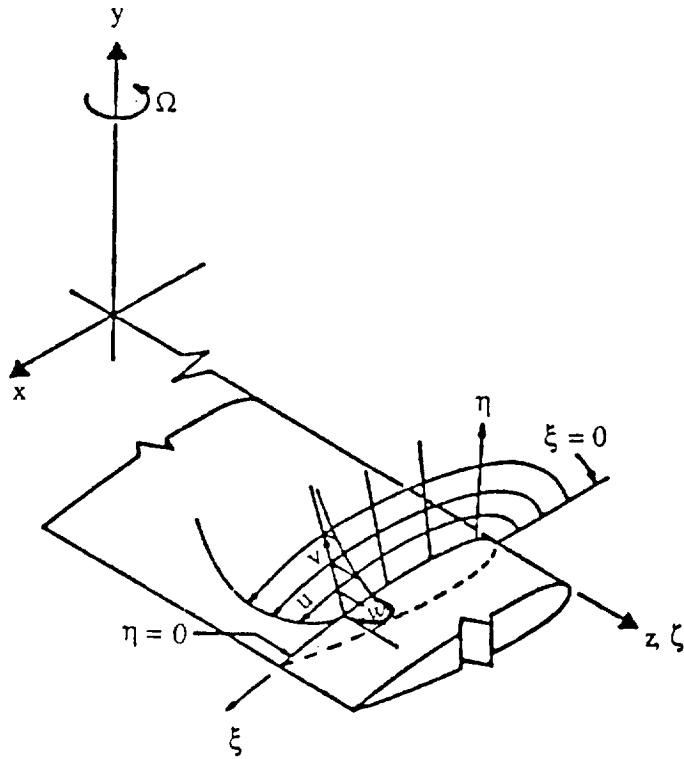
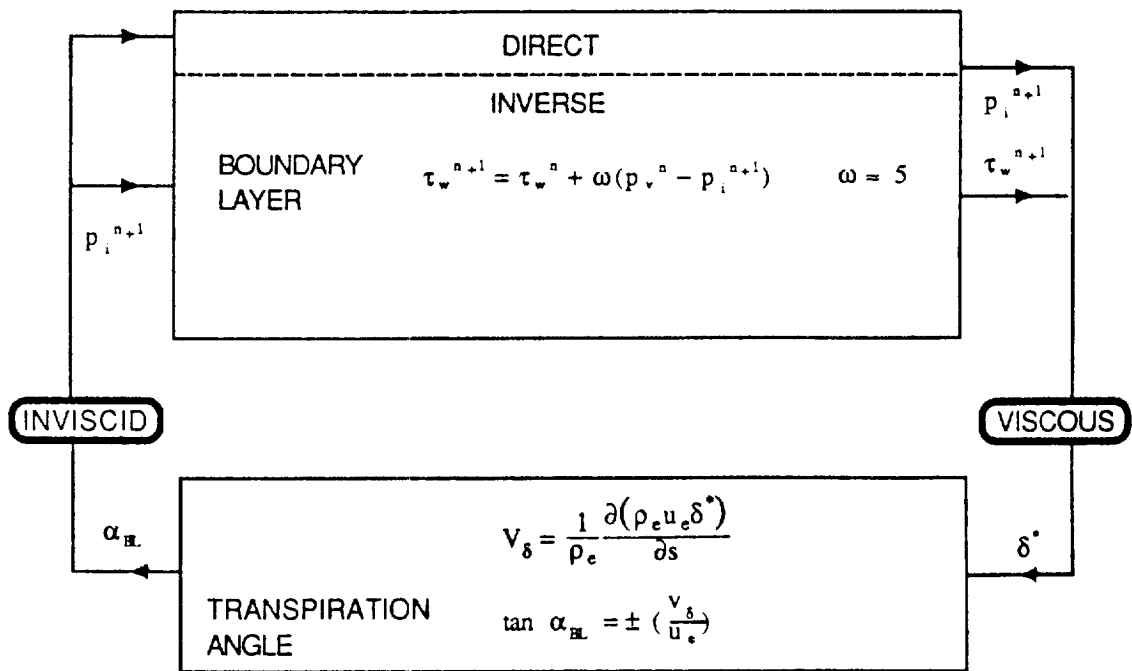Figure 1.– Coordinate systems for a rotating reference frame.

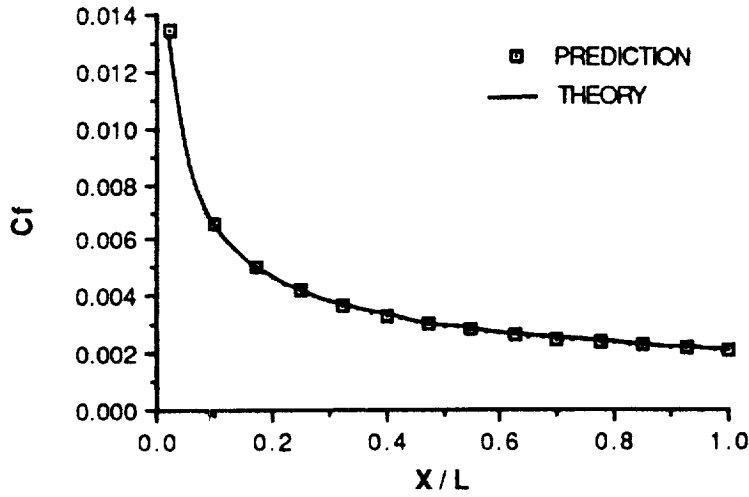Figure 2.– Flowchart of viscous–inviscid interaction.

13

Figure 3.– Comparison of computed local friction coefficients and analytical solution for laminar flow over a flat plate.
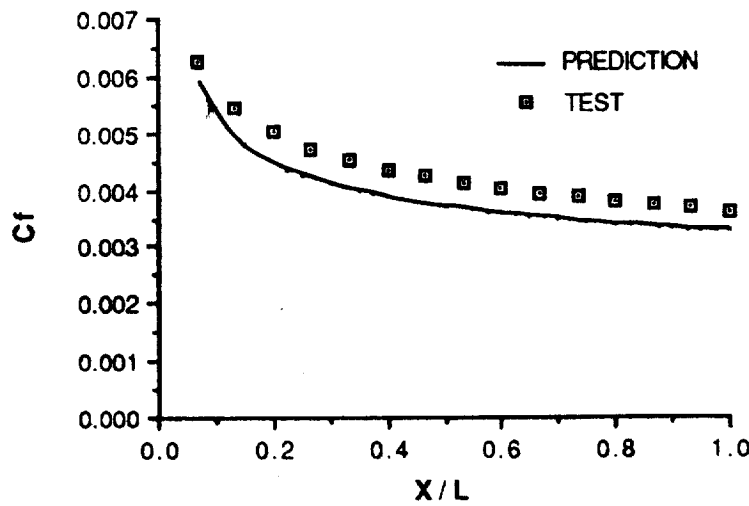

Figure 4.– Comparison of computed local friction coefficients and experimental data for turbulent flow over a flat plate.
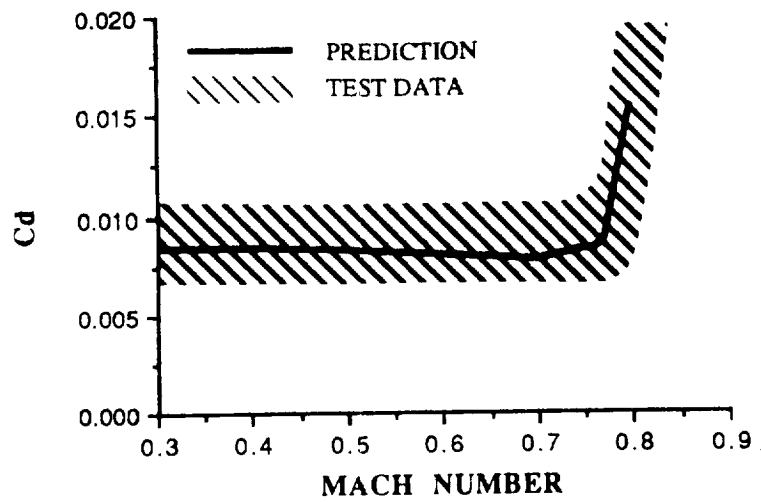
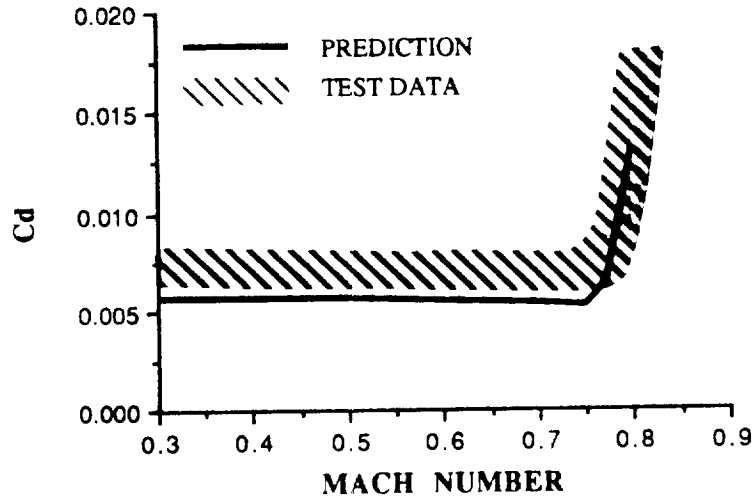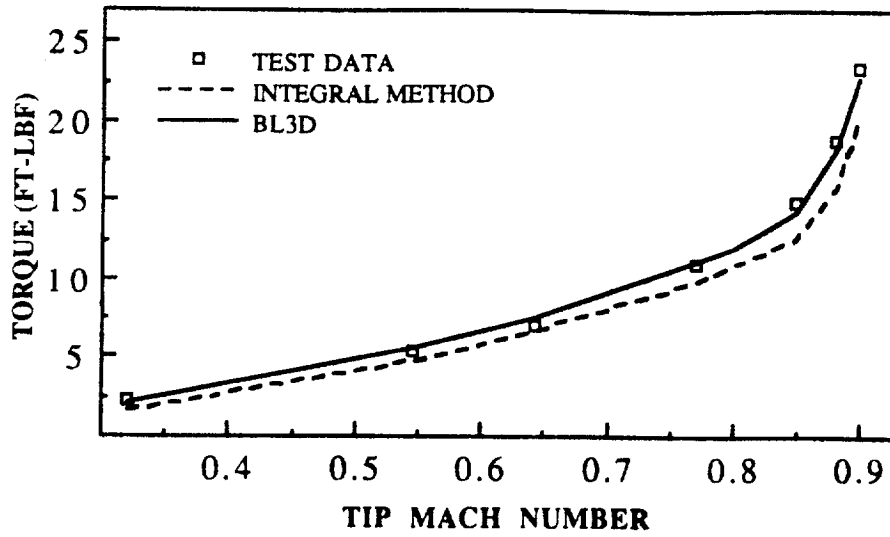Figure 5.– Comparison of computed drag coefficients for the two-dimensional NACA 0012 airfoil flow with a Reynolds number of 10^6.

Figure 6.– Comparison of computed drag coefficients for the two-dimensional NACA 0012 airfoil flow with a Reynolds number of 10^7.

Figure 7.– Comparison of computed torques with test data for the hovering rotor with rectangular blades.
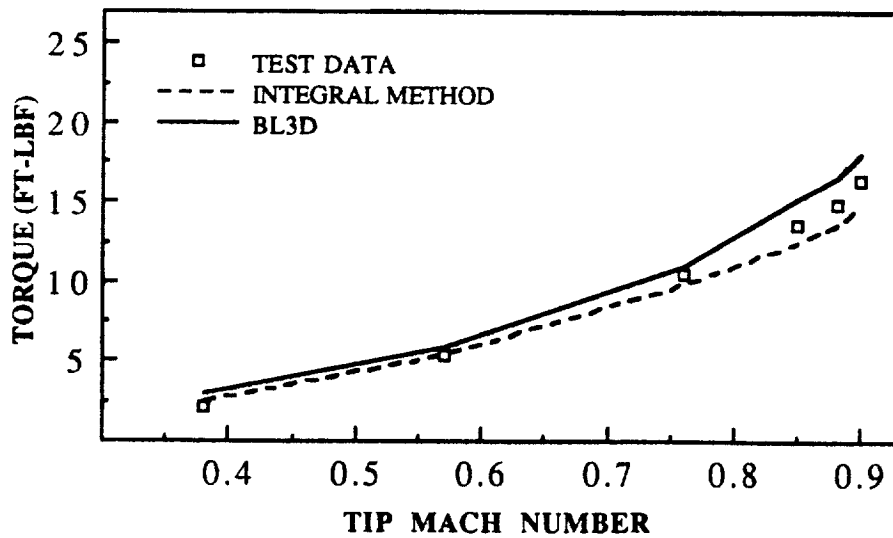
Figure 8.– Comparison of computed torques with test data for the hovering rotor with swept tip blades.

16
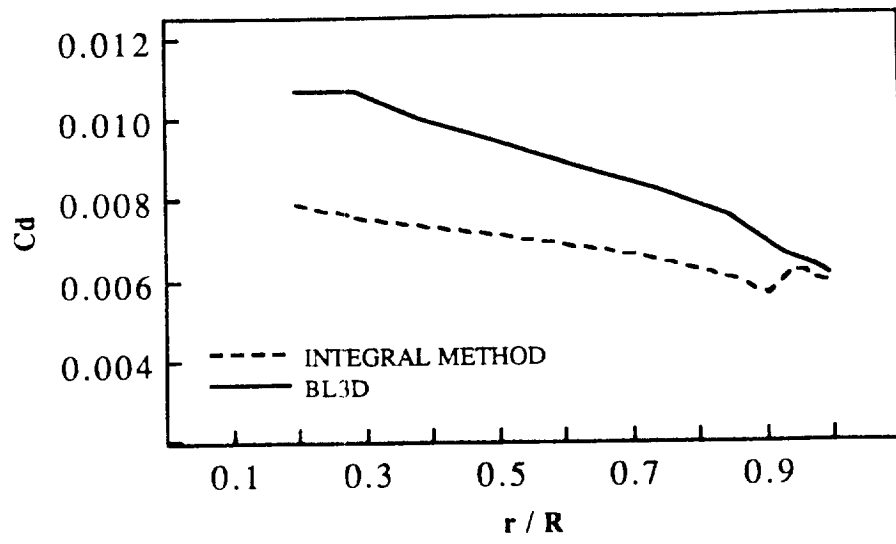
Figure 9.– Comparison of spanwise viscous drag coefficients for the nonlifting hovering rotor with rectangular blades, $M_T = 0.9$.
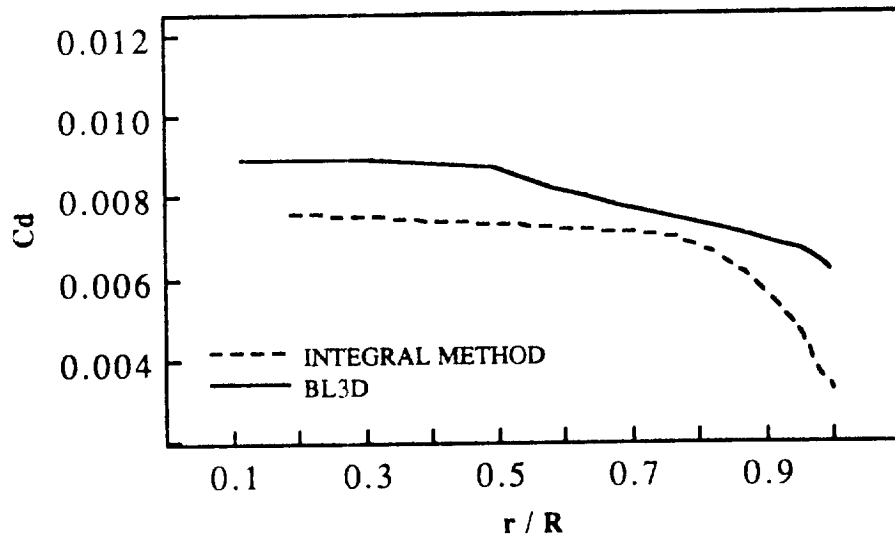
Figure 10.– Comparison of spanwise viscous drag coefficients for the nonlifting hovering rotor with swept tip blades, $M_T = 0.9$.

17
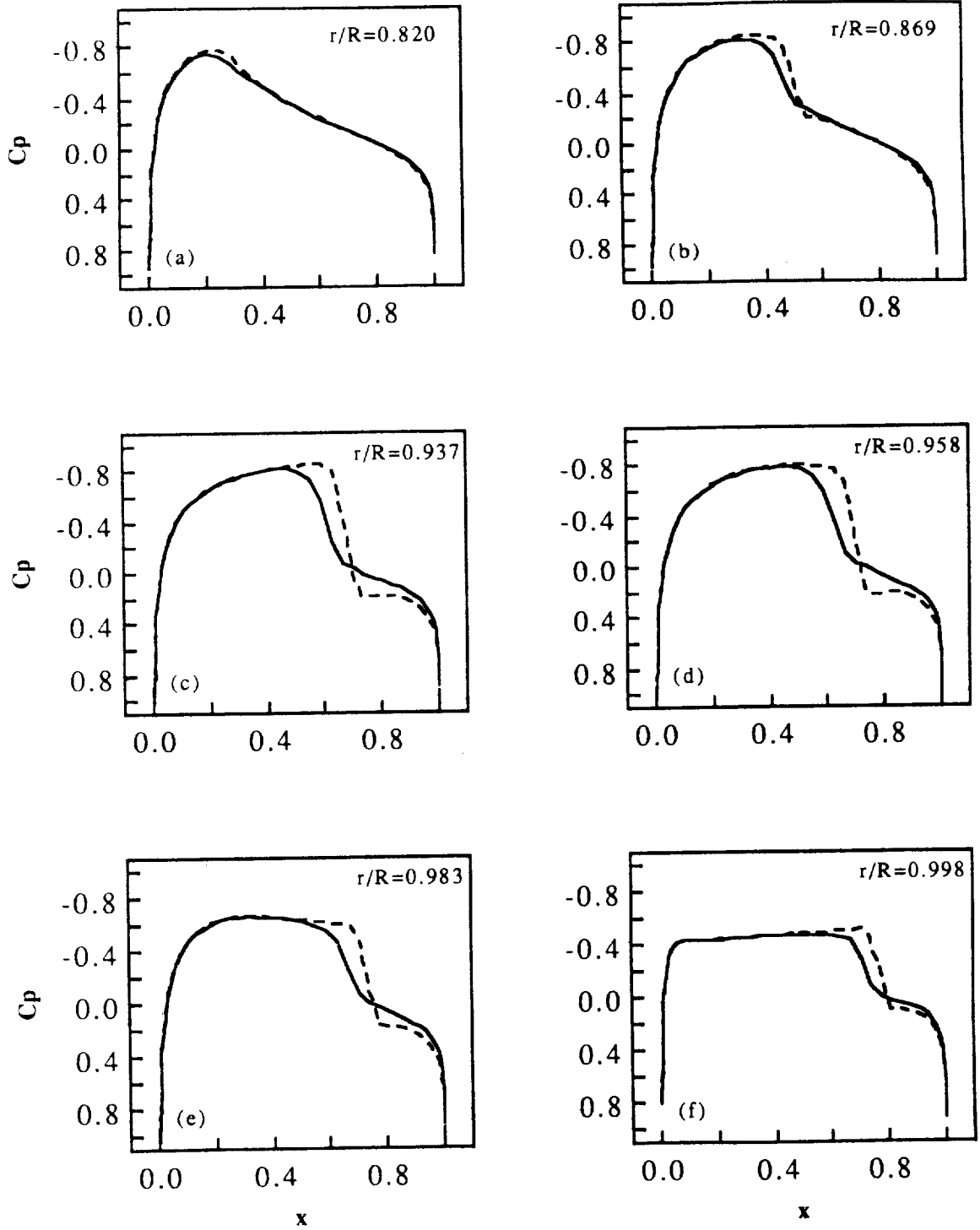
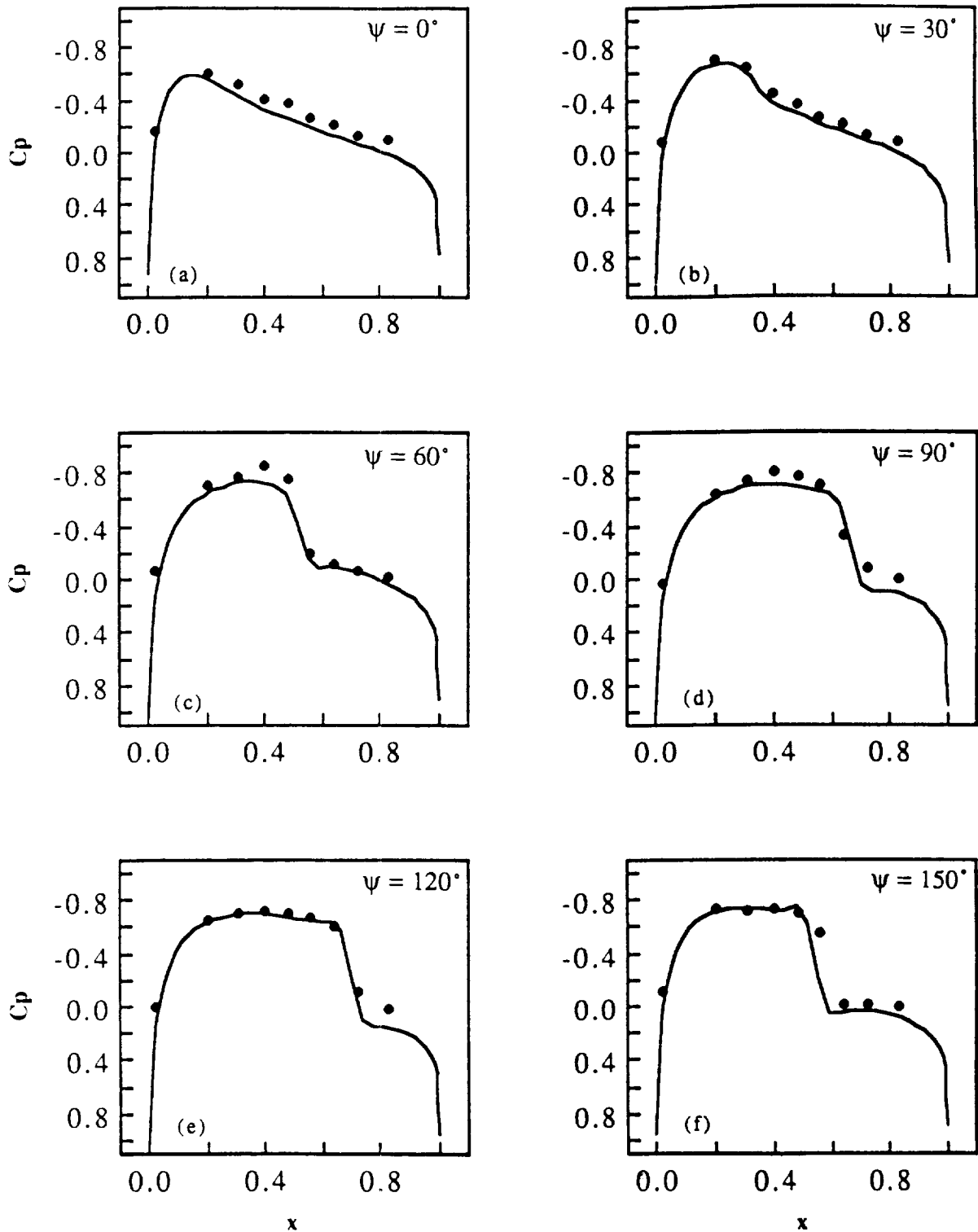Figure 11.– Comparison of pressure coefficients for the nonlifting hovering rotor with rectangular blades, $M_T = 0.925$.

Figure 12.– Surface pressure results for a nonlifting rotor in forward flight, $M_T = 0.763$, AR = 7.125, r/R = 0.876, untwisted rectangular NACA 0012 blade.

1. Report No. NASA TM-102235	2. Government Accession No.	3. Recipient's Catalog No.
4. Title and Subtitle Three-Dimensional Viscous Rotor Flow Calculations Using a Viscous–Inviscid Interaction Approach		5. Report Date February 1990
		6. Performing Organization Code
7. Author(s) Ching S. Chen and John O. Bridgeman* *Woodside Summit Group, Inc., Mountain View, California		8. Performing Organization Report No. A-89246
		10. Work Unit No. 505-61-51
9. Performing Organization Name and Address Ames Research Center Moffett Field, CA 94035-1000		11. Contract or Grant No.
		13. Type of Report and Period Covered Technical Memorandum
12. Sponsoring Agency Name and Address National Aeronautics and Space Administration Washington, DC 20546-0001		14. Sponsoring Agency Code

16. Abstract

A three-dimensional viscous–inviscid interaction analysis has been developed to predict the performance of rotors in hover and in forward flight at subsonic and transonic tip speeds. The analysis solves the full-potential and boundary-layer equations by finite-difference numerical procedures. Calculations were made for several different model rotor configurations. The results were compared with predictions from a two-dimensional integral method and with experimental data. The comparisons show good agreement between predictions and test data.

17. Key Words (Suggested by Author(s)) Viscous rotor flow, Three-dimensional rotor flows, Rotating boundary layer, Viscous–inviscid interaction	18. Distribution Statement Unclassified-Unlimited Subject Category - 02		
19. Security Classif. (of this report) Unclassified	20. Security Classif. (of this page) Unclassified	21. No. of Pages 24	22. Price A02